2022

Enhanced Photo-Fenton Activity Using Magnetic Cu0.5Mn0.5Fe2O4 Nanoparticles as a Recoverable Catalyst for Degrading Organic Contaminants

A. Angkaew

C. Sakulthaew

M. Nimtim

S. Imman

T. Satapanajaru

See next page for additional authors

Angkaew, A.; Sakulthaew, C.; Nimtim, M.; Imman, S.; Satapanajaru, T.; Suriyachai, N.; Kreetachat, T.; Comfort, S.; and Chokejaroenrat, C., "Enhanced Photo-Fenton Activity Using Magnetic Cu0.5Mn0.5Fe2O4 Nanoparticles as a Recoverable Catalyst for Degrading Organic Contaminants" (2022). *Papers in Natural Resources*. 1572.
https://digitalcommons.unl.edu/natrespapers/1572

Authors

A. Angkaew, C. Sakulthaew, M. Nimtim, S. Imman, T. Satapanajaru, N. Suriyachai, T. Kreetachat, S. Comfort, and C. Chokejaroenrat

water

MDPI

Article

Enhanced Photo-Fenton Activity Using Magnetic $Cu_{0.5}Mn_{0.5}Fe_2O_4$ Nanoparticles as a Recoverable Catalyst for Degrading Organic Contaminants

Athaphon Angkaew [1], Chainarong Sakulthaew [2], Matura Nimtim [1], Saksit Imman [3], Tunlawit Satapanajaru [1], Nopparat Suriyachai [3], Torpong Kreetachat [3], Steve Comfort [4] and Chanat Chokejaroenrat [1,*]

[1] Department of Environmental Technology and Management, Faculty of Environment, Kasetsart University, Bangkok 10900, Thailand
[2] Department of Veterinary Technology, Faculty of Veterinary Technology, Kasetsart University, Bangkok 10900, Thailand
[3] Integrated Biorefinery Excellent Center (IBC), School of Energy and Environment, University of Phayao, Phayao 56000, Thailand
[4] School of Natural Resources, University of Nebraska, Lincoln, NE 68583-0915, USA
* Correspondence: chanat.c@ku.ac.th

Abstract: Interest in using various nanoparticle catalysts to activate H_2O_2 with light for organic contaminant and wastewater treatment is steadily increasing. We successfully synthesized magnetically recoverable $Cu_{0.5}Mn_{0.5}Fe_2O_4$ nanoparticles using a simple co-precipitation method followed by melamine-assisted calcination. Material characterization revealed that melamine acted as a coordinating agent during the calcination process that promoted a ferrite structure. Copper (Cu)-substitution effectively decreased material aggregation and promoted catalytic activities. $Cu_{0.5}Mn_{0.5}Fe_2O_4$ nanoparticles showed outstanding catalytic performance on several organic contaminants (87.6–100.0% removal within 2 h). Using oxytetracycline (OTC) as a surrogate wastewater constituent, we found that the hydroxyl radical ($^{\bullet}OH$) and superoxide anions ($^{\bullet}O_2^{-}$) were the active radical species involved in OTC degradation. $Cu_{0.5}Mn_{0.5}Fe_2O_4$ nanoparticles exhibited excellent photo-Fenton catalytic ability in real wastewater and demonstrated high material stability, even after four consecutive uses (i.e., fourth cycle). In a pilot-scale experiment (10 L), we provide proof that our rigorous treatment system was able to remove remnant OTC, TOC, and also any available colloidal particles to only 1 NTU. Ecotoxicity studies using an aquatic plant (*Hydrilla verticillata*) and zooplankton revealed that treated water could be reused in various ratios. Furthermore, at 5% of treated water, rapid leaf recovery and a significant increase in rotifer numbers were reported. These observations support the use of $Cu_{0.5}Mn_{0.5}Fe_2O_4/H_2O_2$/light as an efficient and environmentally friendly catalytic system for treatment of organic contaminants, and a radical generating mechanism is proposed.

Keywords: copper-manganese ferrites; heterogeneous photo-Fenton catalyst; magnetic nanoparticles; organic pollutant removal; toxicological effects

check for updates

Citation: Angkaew, A.; Sakulthaew, C.; Nimtim, M.; Imman, S.; Satapanajaru, T.; Suriyachai, N.; Kreetachat, T.; Comfort, S.; Chokejaroenrat, C. Enhanced Photo-Fenton Activity Using Magnetic $Cu_{0.5}Mn_{0.5}Fe_2O_4$ Nanoparticles as a Recoverable Catalyst for Degrading Organic Contaminants. *Water* **2022**, *14*, 3717. https://doi.org/10.3390/w14223717

Academic Editor: Chengyun Zhou

Received: 5 October 2022
Accepted: 14 November 2022
Published: 17 November 2022

---

1. Introduction

Organic contaminants such as pharmaceuticals, personal care products, agrochemicals, and industrial dyes are ubiquitous in aquatic environments due to their widespread use and general recalcitrance during conventional wastewater treatment [1–3]. While chlorination is commonly used to remove pathogenic microorganisms and several organic contaminants, the generation of unwanted disinfection byproducts (DBPs) such as trihalomethane (THM) and haloacetic acid (HAA) can occur from the chlorine reaction with the organic precursors, i.e., natural organic matter (NOM). Therefore, an efficient and practical approach to removing recalcitrant wastewater contaminants using environmentally friendly treatment technologies is of paramount importance.

Advanced oxidation processes (AOPs) are recognized as established technologies that can degrade persistent contaminants by producing highly reactive oxygen species (ROS) such as $^{\bullet}OH$, $SO_4^{\bullet-}$, $^1O_2$, and $^{\bullet}O_2^-$ [4,5]. Among AOPs, heterogeneous photo-Fenton-like processes have received considerable attention due the reusability of the catalyst and their capability to operate over a wide pH [6,7]. Although many powerful catalysts such as BUC-21 (Fe) [8], $LaFeO_3$/lignin-biochar [9], and Fe/SCN [10] have been created, the recovery of these non-magnetic catalysts could hinder the practical application of the technology. Recently, researchers have used several manganese ferrite nanoparticles ($MnFe_2O_4$) as heterogeneous catalysts to enhance oxidation via electron transfer reactions with ozone [11], persulfate [5], peroxymonosulfate [4], and heterogeneous photo-Fenton reagents [12,13]. The superiority of heterogeneous catalysts is attributable to the existence of various valences in the nanocomposites (Mn^{4+}, Mn^{3+}, Mn^{2+}, Fe^{3+}, and Fe^{2+}) that initiate the synergistic effect between the Mn and Fe redox cycles, and result in better degradation performance [4,14]. In addition, these materials are not only biocompatible but also provide excellent intrinsic magnetism, which facilitates recovery and material reusability from the treated water. Although several researchers have proposed various approaches for synthesizing the $MnFe_2O_4$ nanoparticles using co-precipitation or sol-gel methods, these methods also produce a hematite (α-Fe_2O_3) impurity that reduces the catalyst magnetic properties [15,16]. By using another method such as hydrothermal synthesis [4,17], the obtained bare $MnFe_2O_4$ particles, in turn, possessed too high a level of magneticity that facilitates agglomeration, which reduces the active surface area. To overcome some of these unexpected shortcomings, changing the catalyst physicochemical properties by adding non-metal or metal dopants, or coupling with other semiconductors, or substituting Mn with other metals to construct multicomponent ferrite have been attempted [6,11,18,19].

Copper (Cu) ions appear to be a promising choice to substitute Mn ions to construct $Cu_XMn_{1\text{-}X}Fe_2O_4$ nanoparticles because of their excellent oxygen exchangeability and outstanding capability for electron transfer through the Cu^{2+}/Cu^{1+} redox couple [20]. Because Cu has a smaller ionic radius than Mn, this substitution may create lattice distortions in the spinel structure, which can change the nanoparticle's magnetic and catalytic properties and result in greater oxidative reactivity for pollutant removal [21,22]. These Cu-substitution dosages, including the cation distribution between the octahedral and tetrahedral sites of multicomponent ferrite, are controlling factors for morphological properties and material magnetism [19].

In this work, we synthesized $Cu_{0.5}Mn_{0.5}Fe_2O_4$ nanoparticles by a simple co-precipitation technique followed by melamine-assisted calcination methods. We then documented the nanoparticle's photo-Fenton catalytic activity in degrading several organic pollutants frequently found in treated wastewater effluent, such as oxytetracycline (OTC), enrofloxacin (ENR), sulfadimethoxine (SDM), sulfamethoxazole (SMX), alachlor (ALA), 2,4 dichlorophenoxyacetic acid (2,4 D), atrazine (ATZ), parabens, methylene blue (MB), methyl orange (MO), and crystal violet (CV). The nanoparticle's physicochemical characteristics and reusability were also quantified. Using oxytetracycline as a representative wastewater constituent, we show the effects of organic matter on degradation efficacy. Finally, to test the technology readiness of the nanoparticle, we scaled up experiments and determined the ecotoxicity of the treated water on an aquatic plant (*Hydrilla verticillata*) and zooplankton. Overall results provided proof that our ternary metal ferrite catalyst has great potential as a recoverable catalyst for degrading various organic contaminants and is compatible with conventional wastewater treatment systems.

2. Materials and Methods

Chemicals, vendors, and chemical analyses performed are provided in detail in Supplementary Information (Sections S1–S3 and Table S1).

2.1. Preparation of Catalysts

In an effort to avoid high pressure and temperature, the $Cu_XMn_{1-X}Fe_2O_4$ (x = 0, 0.2, 0.33, 0.5, and 0.66) nanoparticles were synthesized by the co-precipitation method followed by melamine-assisted calcination. In brief, at x = 0.5, the $CuSO_4$ and $MnSO_4{\cdot}H_2O$ concentrations and volumes were equal. For example, to synthesize the $Cu_{0.5}Mn_{0.5}Fe_2O_4$ nanoparticles, we continuously stirred the mixture of 125 mL $CuSO_4$ (0.2 M), 125 mL $MnSO_4{\cdot}H_2O$ (0.2 M), 250 mL $FeCl_3{\cdot}6H_2O$ (0.4 M), and 500 mL deionized water (DI) at 80 °C for 1 h. Then, we separately prepared 8 M NaOH (80 °C) and slowly dripped the base into the mixture for ~1 h to raise the pH to 10.5. After stirring for another hour, we used vacuum filtration to collect the precipitates, washed them with DI water and ethanol several times, and dried at 95 °C for 15 h. To obtain the final product, we mixed 2 g dry particles with 1 g melamine in a crucible and calcined at 550 °C for 3 h.

2.2. Photo-Fenton Catalytic Performance Evaluation

The synthesized catalysts ($Cu_{0.5}Mn_{0.5}Fe_2O_4$) were used in the photo-Fenton catalytic experiments, which were designed to treat organic contaminants such as antibiotics, herbicides, parabens, and industrial dyes. Initially, we investigated the photo-Fenton catalytic activity of $Cu_XMn_{1-X}Fe_2O_4$ nanoparticles (x = 0, 0.2, 0.33, 0.5, and 0.66) using methylene blue (MB) (80 mg/L) as a starting substrate. To obtain the best catalyst composition, we chose the nanoparticle catalyst that performed the best in degrading methylene blue. Unless stated otherwise, all experiments were performed in a 250-mL beaker with 50 mg $Cu_XMn_{1-X}Fe_2O_4$ nanoparticles, which were dispersed in 100 mL of target contaminant (C_0 = 0.1 mM) and stirred in the dark for 30 min to achieve adsorption-desorption equilibrium between the contaminant and catalyst. Then, all flasks were placed in a specifically designed reactor that housed a simulated sunlight source (~12 cm above the water surface) using a commercial 75 W halogen lamp at visible wavelength in the 400–700 nm region. The experiments started immediately after 1 mL of H_2O_2 was injected into the flask following the light irradiation. Temporal 1-mL samples were collected and passed through a 0.45 µm PTFE syringe filter. The 0.7 mL of filtered solution was transferred to an HPLC vial, which held 0.875 mL of methanol as a quencher. The samples were kept in a refrigerator at 4 °C prior to HPLC analysis. For colored contaminants, filtered samples were immediately transferred into a cuvette without quenching and quantified for residual concentration using a spectrophotometer. We measured total organic carbon (TOC) before and after the reaction to quantify TOC removal (%) at 120 min and ensure the complete contaminant degradation.

2.3. Material Adsorption Capacity and pH of Zero Point of Charge (pH_{pzc})

Because most reactions occur on the catalyst surface, the prepared $Cu_{0.5}Mn_{0.5}Fe_2O_4$ nanoparticle adsorption capacity may reveal a key role in the degradation process. In brief, we mixed 30 mL of each contaminant (C_o = 0.1 mM) with 0.12 g of the catalysts in a 40-mL amber glass screw-cap vial and agitated at 190 rpm for up to 3 h using a reciprocating shaker. Temporal samples were periodically collected.

As pH can influence ionic species in solution as well as on the $Cu_{0.5}Mn_{0.5}Fe_2O_4$ nanoparticle surface, we determined the nanoparticle point of zero charge (pH_{pzc}) using a modified method [23]. Firstly, we adjusted the solution pH of each 50 mL sodium chloride solution (0.01 M) to a pH ranging from 2 to 12 using HCl (0.1 M) or NaOH (0.1 M). Then, 0.12 g of $Cu_{0.5}Mn_{0.5}Fe_2O_4$ nanoparticles was added, and the pH was initially measured prior to applying agitation for 48 h. The final pH of each vial was measured and plotted against the designated pH. The intersection of this curve and the initially measured pH curve is the sample pH_{pzc} values.

2.4. Quenching Experiments

To elucidate the catalytic mechanisms and determine the radicals involved during the degradation processes, radical scavenging experiments were performed. Using generalized procedures, oxytetracycline (OTC) degradation was measured but additional radical scavengers were added at a concentration of 100 mM. Specifically, we used tertbutyl alcohol (TBA) as the scavenger for hydroxyl radicals ($^{\bullet}OH$), dimethyl sulfoxide (DMSO) for photogenerated electrons (e^-), and p-benzoquinone (pBQ) as the scavenger for superoxide anions ($^{\bullet}O_2^-$). Once the experiment started, we monitored changes in OTC concentration and compared results with the control (i.e., without scavengers).

2.5. Recycling Experiments

To determine the robustness of the nanoparticle catalyst, we reused the catalyst in four consecutive experiments under identical conditions. Four-cycles of OTC degradation experiments were performed. Each cycle consisted of a 1 h treatment of OTC with the photo-Fenton treatment. After one cycle (60 min), the catalyst was retrieved magnetically from the batch reactor using a neodymium magnet and then washed with water prior to drying at 80 °C for 8 h. The OTC and TOC removal percentages and leaching metal contents (i.e., Cu, Mn, and Fe) from each cycle were recorded. After the fourth cycle, these materials were characterized using XPS for determining changes in metal oxidation states.

2.6. Effect of Real Water

To investigate the applicability of the system to treat OTC in actual water samples, we spiked OTC to an initial concentration of 0.1 mM in the waters collected from the municipal wastewater treatment plant at Kasetsart University (Bangkok, Thailand) (13.855360, 100.570124), actual discharge of domestic wastewater (Wastewater Collection Station #1: 13.854984, 100.570327, and Wastewater Collection Station #2: 13.822234, 100.471106), and canal water (13.820820, 100.469383). The basic water quality parameters were determined immediately after collection, and again after adding OTC, and finally, after treating (Table S2). Then, the same sampling protocol for OTC treatment and analysis were followed.

2.7. Pilot-Scale Experiment

To determine whether our technology could treat contaminated water more efficiently and potentially be scaled up for commercial use, we conducted a pilot-scale experiment. Here, the photocatalytic experiment was scaled up 100-fold (i.e., 100 mL to 10 L). The experiment was performed in a glass container (44 × 19 × 21 cm; W × L × H) equipped with three 75 W halogen lamps, which were aligned perpendicular to the lamp light direction and symmetrically located along the water surface. Initially, we added 2 g of catalyst into 10 L of the collected wastewater (Wastewater Collection Station #3: 13.854592, 100.570231) and continuously stirred for 30 min to reach catalyst adsorption–desorption equilibrium. Fifty mL of H_2O_2 was added to the solution followed by light irradiation. At the predetermined intervals, 40 mL of solution was transferred into an EPA vial and the catalyst was magnetically extracted to allow solution turbidity measurement. After treating for 6 h, we removed all catalysts and rested the treated water to remain stabilized at room temperature for 72 h for successive evaluations of the toxicological impact on an aquatic plant (*Hydrilla verticillata*) and zooplankton.

2.8. Toxicological Evaluation

To test the ecotoxicity of the treated wastewater, *Hydrilla verticillata* was selected as a representative aquatic submerged plant. Using water collected at Wastewater Collection Station #3, we filtered the water with a 65 µm plankton net to remove zooplankton and used this water as natural receiving water. Treated water from the previous experiments was split into either 250, 500, or 750 mL aliquots and mixed with the filtered wastewater for a total of 5 L. These mixtures of treated and untreated water were placed in 10 L water containers, and labeled as 5%, 10%, and 15%. The experiments were performed in duplicate. These water mixtures were used in the following experiment. Changes in *Hydrilla verticillata* and the zooplankton community in the water mixtures were compared with the untreated water (Control; 0%). Approximately 10 g of *Hydrilla verticillata* (wet weight) was carefully selected and raised in simulated natural water for 3 d at room temperature to ensure that these plants were maintained in healthy conditions. Then, these acclimated plants were exposed to each water mixture for up to 20 d. At 5 d, representative leaves were collected from the containers, rinsed gently with water, and visually observed using a stereomicroscope.

All zooplankton related experiments conducted in this study followed the animal research ethical approval obtained from Kasetsart University (ID# ACKU64-VTN-016). To explore changes in the zooplankton community after exposure to the water mixtures (i.e., 0, 5, 10, and 15%, v/v), we filtered natural zooplankton using a plankton net from 160 L of Wastewater Collection Station #3 collected at <45 cm below the surface water. These zooplankton were divided into eight portions and placed in water tanks containing different treated water mixtures (0–15%). Each experimental unit was performed in duplicates. After 3 d of exposure, we used a plankton net to collect zooplankton from each container, transferred to a 100-mL bottle, and added 10 mL of ethanol to preserve them for further analysis. Changes in zooplankton numbers were assessed by taking repeated observations on 1 mL sub-sample and counted using a Sedgewick–Rafter counting chamber. Identification of zooplankton was classified up to the genus level.

3. Results and Discussion

3.1. Material Characterization

Two synthesized catalysts' purity and crystallinity were investigated using XRD (i.e., with and without melamine addition). By adding melamine, the $Cu_{0.5}Mn_{0.5}Fe_2O_4$ nanoparticle diffraction peaks located at 18.3°, 30.0°, 35.4°, 37.0°, 43.0°, 53.3°, 56.8°, and 62.4° were well indexed to the (111), (220), (311), (222), (400), (422), (511), and (440) crystal plane of the $Cu_{0.5}Mn_{0.5}Fe_2O_4$ spinel structure (JCPDS No. 74-2072) (Figure 1a). The X-ray mapping images and the elemental composition analysis using energy dispersive spectrometry (EDS) revealed that the Cu elements were distributed in the samples and the atomic composition of Cu and Mn was relatively close (Figure S1). However, the crystallite size calculation based on Debye–Scherrer's equation revealed $Cu_{0.5}Mn_{0.5}Fe_2O_4$ nanoparticles in a smaller size compared to $MnFe_2O_4$ (35.7 vs. 29.8 nm). This was because Cu^{2+} ions had distorted the $MnFe_2O_4$ spinel structures, resulting in decreasing crystallite size and more active surface area. With melamine addition, XRD peaks showed much higher $Cu_{0.5}Mn_{0.5}Fe_2O_4$ intensity with no hematite (α-Fe_2O_3) impurity, confirming the importance of adding melamine during $Cu_{0.5}Mn_{0.5}Fe_2O_4$ nanoparticle synthesis (Figure 1a). To further explain the melamine role, we used FTIR and XPS to determine the surface chemical composition and compare the catalyst spectral changes with and without melamine addition, which are provided in detail in the Supplementary Information (Section S4 and Figure S2).

To verify the catalyst magnetic property, we examined their M-H hysteresis loop. Results showed that the $Cu_{0.5}Mn_{0.5}Fe_2O_4$ saturation magnetization (Ms) values significantly increased by 442% compared to the prepared catalyst without melamine addition and almost mirrored that of $MnFe_2O_4$ (Figure 1b). Although the $Cu_{0.5}Mn_{0.5}Fe_2O_4$ and $MnFe_2O_4$ Ms values were slightly different, we observed much less $Cu_{0.5}Mn_{0.5}Fe_2O_4$ agglomeration (Figure 1b and its inset photos before applying magnetization). This can be explained by (1) a smaller crystallite size, and (2) the Cu distribution in the spinel ferrite that reduced magnetic interaction between particles. However, the $Cu_{0.5}Mn_{0.5}Fe_2O_4$ showed rapid recovery using a magnet within a few minutes (Figure 1b inset photo). The magnetism improvement was mainly from the α-Fe_2O_3 disappearance after recrystallization as the α-Fe_2O_3 oriented in the antiparallel position, which exhibited weakly ferromagnetic behavior at room temperature [24] (Figure 1a).

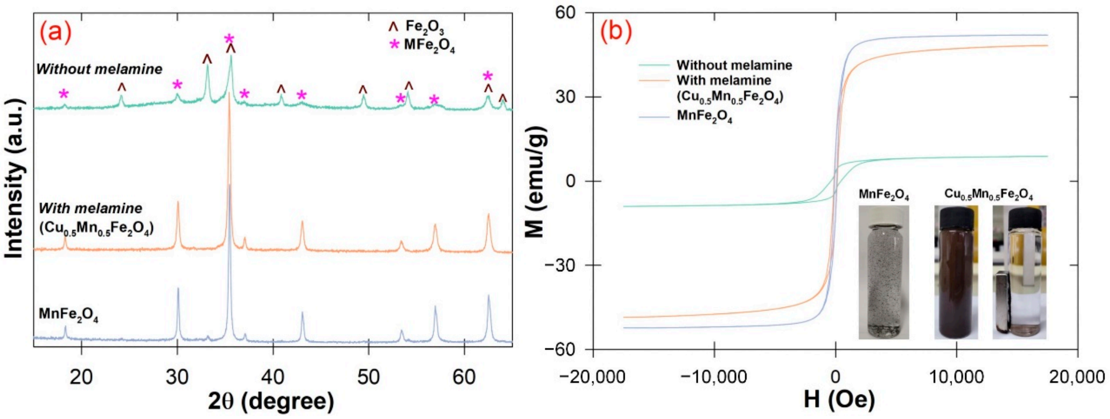

Figure 1. The prepared catalysts: (**a**) XRD, and (**b**) VSM (inset photo illustrated the magnetic separation).

Furthermore, the UV-Vis diffuse reflectance spectra revealed that the $Cu_{0.5}Mn_{0.5}Fe_2O_4$ exhibited a broad absorption in all regions of UV and visible light and, by plotting $(\alpha h\nu)^2$ versus photon energy ($h\nu$) (i.e., Tauc's equation), the $Cu_{0.5}Mn_{0.5}Fe_2O_4$ bandgap energy (E_g) was found to be 1.7 eV, confirming that the catalyst can be activated under visible light irradiation (Figure S3a,b).

The $Cu_{0.5}Mn_{0.5}Fe_2O_4$ nanoparticle morphological structures, surface textural, and size were characterized using SEM and TEM. Most particles had octahedral morphology (Figure 2a–c). Compared with other synthesis approaches (e.g., solvothermal, Sun et al. [21]; sol-gel autocombustion, Velinov et al. [16]; and co-precipitation followed by annealing treatment, Yang et al. [25]); our $Cu_{0.5}Mn_{0.5}Fe_2O_4$ had much higher crystalline morphology. Noticeably in both SEM and magnified TEM images, small particles were well-distributed among larger particles, which further confirmed the impeccable melamine-assisted calcination, allowing rapid electron transfer and efficient photocatalytic activity (Figure 2a–c). The HRTEM image also revealed lattice fringe spacing of 0.25 nm corresponded to the (311) crystal plane (Figure 2d).

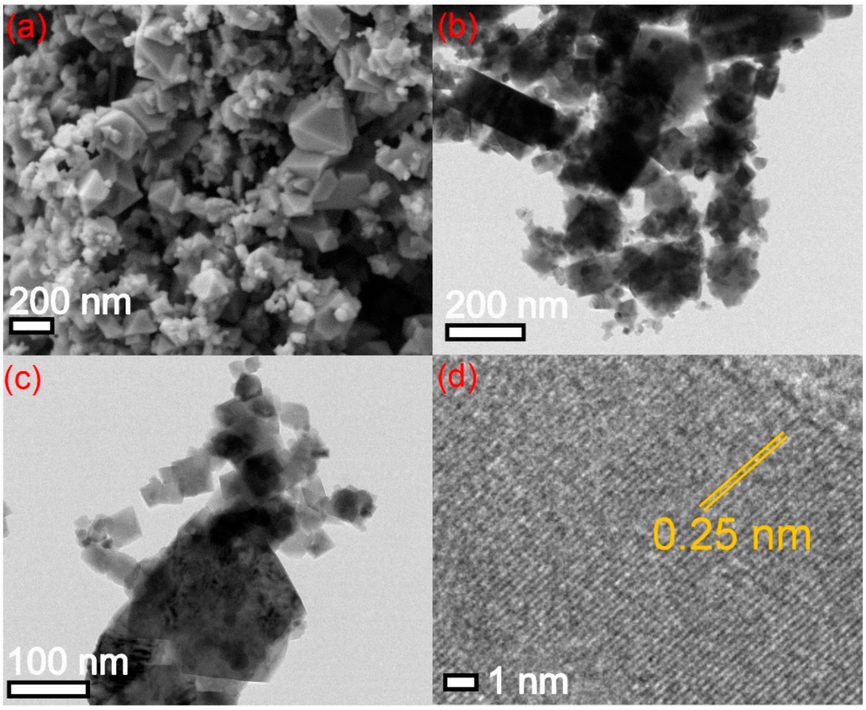

Figure 2. (**a**) SEM, (**b**,**c**) TEM, (**d**) HRTEM images of $Cu_{0.5}Mn_{0.5}Fe_2O_4$ nanoparticles.

3.2. Degradation Performance

Because the Cu-substitution dosages for synthesizing $Cu_XMn_{1\text{-}X}Fe_2O_4$ ferrites can alter their physiochemical characteristic, which can directly affect catalyst applicability, we prepared four $Cu_XMn_{1\text{-}X}Fe_2O_4$ catalysts at different compositions (x = 0.2, 0.33, 0.5, and 0.66) and determined the photo-Fenton efficiency on methylene blue (MB). Results showed that Cu-Mn ferrites have better catalytic performance as compared to $MnFe_2O_4$ while $Cu_{0.5}Mn_{0.5}Fe_2O_4$ provided the highest degradation performance (Figure S4). Besides decreasing the material agglomeration (Figure 1b), Cu-substitution can also provide active Cu ion species that can promote the photo-Fenton reactions [Equations (1) and (2)] [1], and can improve its catalytic activity by synergistic effects between metal valences (i.e., Mn, Fe, and Cu) [Equations (3)–(5)] [7,21].

$$Cu^{2+} + h\nu + e^- \rightarrow Cu^+ \tag{1}$$

$$Cu^+ + H_2O_2 \rightarrow Cu^{2+} + {}^{\bullet}OH + OH^- \tag{2}$$

$$Mn^{3+} + Fe^{2+} \rightarrow Mn^{2+} + Fe^{3+}\ E_0 = 0.74\ V \tag{3}$$

$$Fe^{3+} + Cu^+ \rightarrow Fe^{2+} + Cu^{2+}\ E_0 = 0.60\ V \tag{4}$$

$$Mn^{3+} + Cu^+ \rightarrow Mn^{2+} + Cu^{2+}\ E_0 = 1.34\ V \tag{5}$$

The results showed that the differences in methylene blue degradation efficiency were minimal between x = 0.33 and x = 0.66 (Figure S4). Moreover, further adding Cu would decrease the recovery efficiency as it reduces the catalyst Ms values [19]. Therefore, we selected $Cu_{0.5}Mn_{0.5}Fe_2O_4$ for all successive experiments.

One way to further investigate the $Cu_{0.5}Mn_{0.5}Fe_2O_4$ catalytic performance is through both contaminant and TOC removal under different treatment systems. By using oxytetracycline (OTC) as a contaminant surrogate, we found that only 50% of OTC concentration and 8% of TOC content were removed by H_2O_2 alone due to its low redox potential (E_0 = 1.76 V) [26] (Figure 3a,b). Interestingly, the OTC transformed faster in the H_2O_2/light system but no changes in TOC removal were observed, indicating that the generated ${}^{\bullet}OH$ was able to degrade OTC but not mineralize (i.e., → CO_2). When we used $Cu_{0.5}Mn_{0.5}Fe_2O_4$ to activate H_2O_2, the OTC removal was not as strong as compared to the H_2O_2/light system, but the TOC removal efficiency increased by 16%. This increase was mainly due to the metal ions from $Cu_{0.5}Mn_{0.5}Fe_2O_4$ that were able to initiate other reactive oxygen species (ROS) such as superoxide radicals (${}^{\bullet}O_2{}^-$) and singlet oxygen (${}^1O_2$) [Equations (6)–(8)] [13,27,28].

$$M^{(n+1)+} + H_2O_2 \rightarrow M^{n+} + {}^{\bullet}OOH + H^+ \tag{6}$$

$${}^{\bullet}OOH \rightarrow {}^{\bullet}O_2{}^- + H^+ \tag{7}$$

$${}^{\bullet}OOH + {}^{\bullet}O_2{}^- \rightarrow {}^1O_2 + OOH^- \tag{8}$$

Notably, a much faster OTC removal efficiency was observed from the $Cu_{0.5}Mn_{0.5}Fe_2O_4$/H_2O_2 system under solar light irradiation. This system was able to completely degrade OTC within 45 min and removed up to 58% of TOC. Such results indicated that $Cu_{0.5}Mn_{0.5}Fe_2O_4$ can provide dual beneficial effects from both light irradiation and H_2O_2 activation in the photo-Fenton reaction, thereby promoting reactive oxygen species during oxidation processes [Equations (1) and (9)–(12)] [1,13,29] (Figure S3b).

$$Cu_{0.5}Mn_{0.5}Fe_2O_4 + h\nu \rightarrow e^- + h^+ \tag{9}$$

$$e^- + O_2 \rightarrow {}^{\bullet}O_2 \tag{10}$$

$$e^- + H_2O_2 \rightarrow {}^{\bullet}OH + OH^- \tag{11}$$

$$Fe^{3+} + H_2O + h\nu \rightarrow Fe^{2+} + {}^{\bullet}OH + H^+ \tag{12}$$

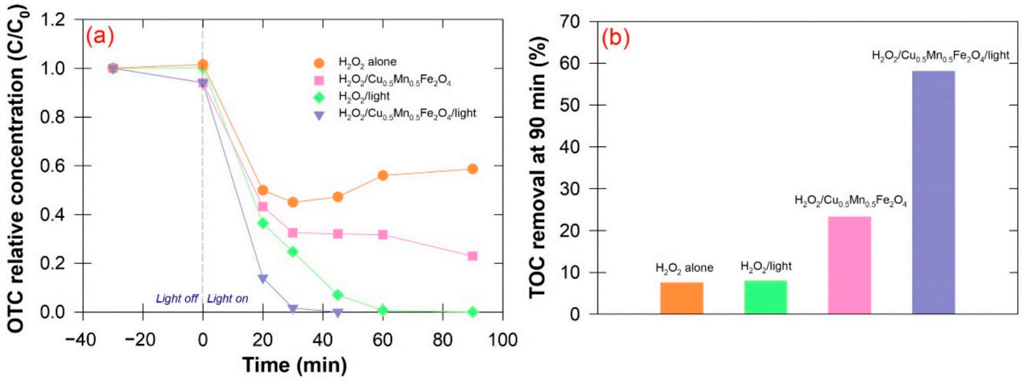

Figure 3. (**a**) Temporal changes in OTC concentration and (**b**) TOC removal efficiency under different conditions (Experimental conditions: $[OTC]_0$ = 0.1 mM, $[H_2O_2]$ = 97.89 mM, catalyst loading = 0.5 g/L).

To ensure that the $Cu_{0.5}Mn_{0.5}Fe_2O_4/H_2O_2$/light system is well-suited to work with various organic pollutants, we conducted batch experiments using an individual pollutant as a starting substrate under neutral pH. Temporal changes in pollutant concentrations were also monitored to determine degradation rates, which fit pseudo-first order kinetics with results ranging from 0.009 min^{-1} (methyl orange, MO) to 0.086 min^{-1} (OTC) (Figure 4a). Our treatment system removed pollutants with 87.6% to 100.0% efficiency within 120 min while TOC removal efficiencies ranged between 28.2% and 67.9% (Figure 4a). The one exception to these findings occurred with methylene orange (MO)—an anionic dye widely used in the textile industry—where the MO reduction was only 71.4% with a 16.1% TOC removal, indicating that differences in pollutant formal charge versus catalyst surface charge can influence removal efficiencies.

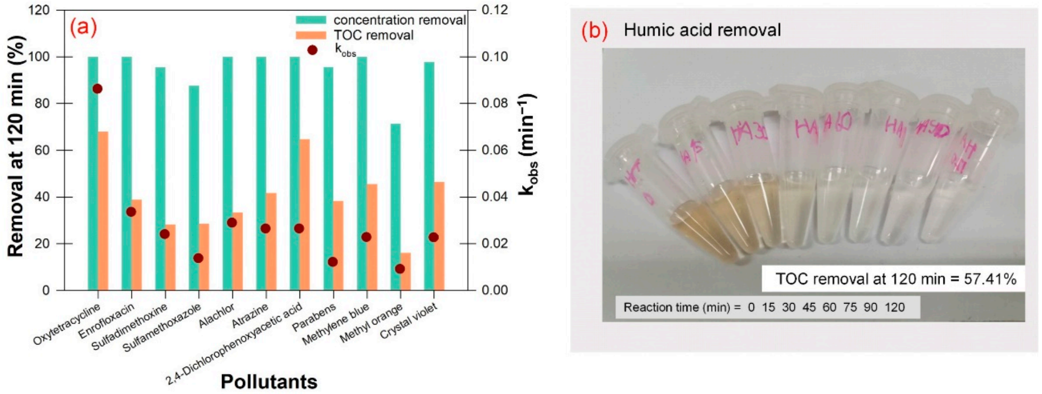

Figure 4. (**a**) The organic pollutant removal efficiencies and their observed kinetic rate constants (k_{obs}), and (**b**) the removal of 100 mg/L humic acid using $Cu_{0.5}Mn_{0.5}Fe_2O_4/H_2O_2$/light system (Conditions: $[H_2O_2]$ = 97.89 mM, catalyst loading = 0.5 g/L, $[pollutant]_0$ = 0.1 mM).

The effect of charge interactions between the catalyst and contaminants was further investigated by determining the $Cu_{0.5}Mn_{0.5}Fe_2O_4$ nanoparticles pH of zero-point charge (pH_{pzc}) as well as the adsorption potential of the various contaminants following 60 min of contact. Results showed that up to 55% OTC was removed while MO and other pollutants were removed <5% except the enrofloxacin (ENR) (10%) (Figure S5). The higher adsorption efficiency can be expected as the adsorbed OTC molecules were close to the generated radicals ((Figures 4a and S5a). Although the adsorption efficiency depends on the adsorbent amount, previous research has shown that copious adsorbent (>1 g/L) can lead to self-aggregation and lead to a decrease in surface area active sites [30]. Furthermore, our results confirmed that using a 0.5 g/L catalyst dose was sufficient for removing OTC under photo-Fenton process (Figure 4a). The MO reduction, on the other hand, was difficult to remove either from degradation or adsorption due to the adsorbate–adsorbent charge interaction. At this working condition (pH = 7), the $Cu_{0.5}Mn_{0.5}Fe_2O_4$ (pH_{pzc} = 6.0) and the MO molecule (MO_{pKa} = 3.47) possessed the same negative charge, which sustained a repulsive electrostatic interaction (Figure S5b). Unlike the OTC molecule, which is always present in neutral form (OTC_{pKa2} = 7.49), the adsorption favorably occurs, confirming the OTC fast degradation rate as the adsorption simultaneously occurs followed by the photo-Fenton process [31] (Figure 4a).

By using humic acid (HA) as a representative of natural organic matter, we tested our system under more environmentally relevant conditions. In the treatment of HA, TOC content and color were monitored (Figure 4b). Results showed that, up to 57.41% HA was removed and the solution color turned clear within 120 min while, in the adsorption study, up to 35% was removed, which was second to the OTC removal ((Figures 4b and S5a). This can be explained by the natural HA form that is mostly deprotonated. Therefore, in the HA abundant solution, the solution pH was lower than the $Cu_{0.5}Mn_{0.5}Fe_2O_4$ pH_{pzc}, making the catalyst surface positively charged, enhancing both adsorption behavior and consequently increasing photo-Fenton performance (Figure 4b and Figure S5a,b). Moreover, besides the carboxylic groups that can form the surface-OH bonding with the catalyst surface, numerously located phenolic groups on the HA surface can initiate the hydrophobic forces between the catalyst surface and the unprotonated phenolic groups. A further explanation for the fast degradation was these organic radical formations (i.e., $R^{\bullet}$, $ROO^{\bullet}$) [Equations (13)–(16)] [29] which participated in generating reactive radicals (i.e., ${}^{\bullet}O_2^{-}$, ${}^{\bullet}OH$), which could be involved with further degradation of these organic contaminants [Equations (7) and (17)] [1].

$$RH + {}^{\bullet}OH \rightarrow R^{\bullet} + H_2O \tag{13}$$

$$R^{\bullet} + O_2 \rightarrow ROO^{\bullet} \tag{14}$$

$$ROO^{\bullet} + RH \rightarrow ROOH + R^{\bullet} \tag{15}$$

$$ROO^{\bullet} + H_2O \rightarrow ROH + {}^{\bullet}OOH \tag{16}$$

$$H_2O_2 + {}^{\bullet}OOH \rightarrow O_2 + {}^{\bullet}OH + H_2O \tag{17}$$

3.3. Photo-Fenton Mechanism

The photo-Fenton process is known to generate reactive radical species during pollutant degradation. By using various radical scavengers, the roles of these species were investigated. Compared to the control, results showed that these radical scavengers inhibited OTC removal in the following order: pBQ > TBA > DMSO; this indicates that ${}^{\bullet}O_2^{-}$ and ${}^{\bullet}OH$ were the predominant active species (Figure 5a). Moreover, OTC degradation was impeded in the presence of DMSO, an effective scavenger for photogenerated electrons (e^-). This result clearly confirmed that the e^- could also act as a precursor during the photo-Fenton process, which would be one additional route for generating subsequence ${}^{\bullet}O_2^{-}$ and ${}^{\bullet}OH$ as discussed earlier [Equations (9)–(11)].

To obtain in-depth information on the catalytic mechanism, we used the XPS spectra to confirm the $Cu_{0.5}Mn_{0.5}Fe_2O_4$ elemental composition and metal oxidation states before and after treatment in the photo-Fenton process. Mn 2p spectra were composed of two main binding energy peaks at ~641.0 (Mn $2p_{3/2}$) and ~652.5 eV (Mn $2p_{1/2}$). The coexistence of Mn ion multi-valence states was evidenced from the three binding energy peaks at ~639.1, ~641.2, and ~643.1 eV in Mn $2p_{3/2}$ and ~650.8, ~652.9, and ~654.8 eV in Mn $2p_{1/2}$, corresponding to Mn^{2+}, Mn^{3+}, and Mn^{4+} [18,32] (Figure 5b). After use in the treatment, the Mn^{3+} decreased from 63.1% to 55.5%, the Mn^{2+} increased from 16.5% to 18.6%, and the Mn^{4+} increased from 20.4% to 25.9%, confirming the Mn^{3+} ions having a key role in the ${}^{\bullet}OOH$ and ${}^{\bullet}OH$ generation (Figure 5b). The continuous interconversion among Mn^{n+} states provided proof that H_2O_2 can be constantly supplied with Mn electron transfer, in which H_2O_2 would be decomposed to ${}^{\bullet}OH$, thereby enhancing the pollutant degradation efficiency [Equations (6) and (18)–(23)] [27,33,34].

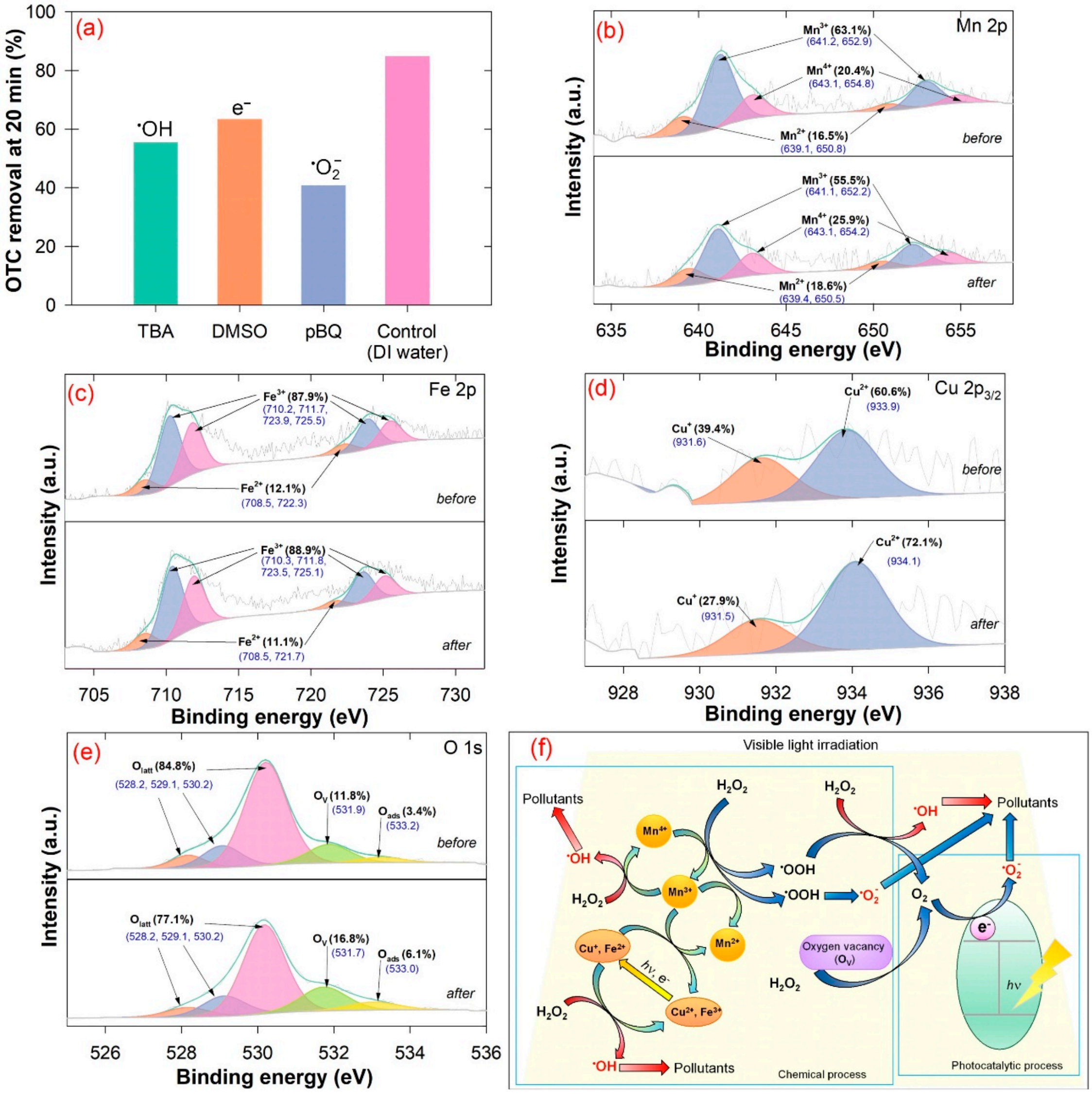

Figure 5. (**a**) OTC removal efficiency using $Cu_{0.5}Mn_{0.5}Fe_2O_4/H_2O_2$/light system with different quenchers (Conditions: $[OTC]_0$ = 0.1 mM, $[H_2O_2]$ = 97.89 mM, [quencher] = 100 mM, catalyst loading = 0.5 g/L, reaction time = 20 min), $Cu_{0.5}Mn_{0.5}Fe_2O_4$ nanoparticle (**b**) Mn 2p, (**c**) Fe 2p, (**d**) Cu 2p, and (**e**) O 1s XPS spectra before and after photo-Fenton reaction, and (**f**) the photo-Fenton radical formation mechanisms during the treatment.

$$Mn^{2+} + H_2O_2 \rightarrow Mn^{3+} + {}^{\bullet}OH + OH^- \quad (18)$$

$$Mn^{3+} + H_2O_2 \rightarrow Mn^{2+} + {}^{\bullet}OOH + H^+ \quad (19)$$

$$Mn^{3+} + H_2O_2 \rightarrow Mn^{4+} + {}^{\bullet}OH + HO^- \quad (20)$$

$$Mn^{4+} + H_2O_2 \rightarrow Mn^{3+} + {}^{\bullet}OOH + H^+ \quad (21)$$

$$Mn^{3+} + {}^{\bullet}OOH \rightarrow Mn^{2+} + O_2 + H^+ \quad (22)$$

$$Mn^{3+} + {}^{\bullet}OH \rightarrow Mn^{4+} + OH^- \quad (23)$$

Fe 2p spectra revealed two binding energy peaks at ~710.5 and ~711.7 eV (Fe $2p_{3/2}$) and 723.9 eV, 725.5 eV (Fe $2p_{1/2}$), corresponding to Fe^{3+} while the deconvoluted peaks of ~708.5 and ~722.3 eV were ascribed to the Fe^{2+} [35] (Figure 5c). Results revealed the decrease in Fe^{2+} and the increase in Fe^{3+} after use in the treatment, indicating that Fe^{2+}

ions were oxidized to Fe^{3+} ions via the Fenton reaction and induced $^{\bullet}OH$ formation [Equation (24)] [18]. Although stable Fe^{3+} can form the surface oxide layer on $Cu_{0.5}Mn_{0.5}Fe_2O_4$, which can impede further H_2O_2 activation, with light irradiation, Fe^{3+} can still proceed to regenerate Fe^{2+}, $^{\bullet}OH$, and $^{\bullet}OOH$ [Equations (12) and (25)] [25,36].

$$Fe^{2+} + H_2O_2 \rightarrow Fe^{3+} + {}^{\bullet}OH + HO^{-} \tag{24}$$

$$Fe^{3+} + H_2O_2 \rightarrow Fe^{2+} + {}^{\bullet}OOH + H^{+} \tag{25}$$

The Cu $2p_{3/2}$ peaks at binding energy ~931.6 were identified as Cu^{1+} while the peaks at ~933.9 were identified as Cu^{2+} [7,37] (Figure 5d). Here, a 11.5% decrease in Cu^{2+} composition after treatment was observed, signifying that the Cu^{1+} oxidation had occurred. This change can be inferred from the continuous cyclic transformation among these two Cu states once activated with H_2O_2, resulting in $^{\bullet}OH$ generation [Equation (2)]. Moreover, the electron transfer between these Mn, Fe, and Cu redox reactions [Equations (3)–(5)] can always favorably occur, which improves electron transfer and redox cycling of metal ions. This can lead to an oxygen vacancy and promote degradation via $^{\bullet}OH$ generation [20,21,38].

In the O 1s spectra, three peaks at binding energy ~528.2, ~529.1 and ~530.2 eV were assigned to the surface lattice oxygen of metal oxides (i.e., Fe–O, Mn–O and Cu–O; O_{latt}) [12,37] (Figure 5e). The deconvoluted peak at 531.9 eV was identified as the oxygen vacancy (O_V) while the peak at 533.2 eV was attributed to the adsorbed oxygen (O_{ads}) and/or adsorbed molecular H_2O [13,21]. After use in the treatment, a decrease in O_{latt} (84.8% to 77.1%) coincided with an increase in O_V (11.8% to 16.8%), indicating that O_{latt} was released, possibly to maintain the electric neutrality of transformed metal ions [39,40] (Figure 5e). Once these phenomena happened, the increase in O_V could result in multiplying nanoparticle active sites for activating chemisorbed oxygen, which improved the H_2O_2 utilization rate and later facilitated the $^{\bullet}OH$ and $^1O_2$ generation [41,42].

Based on the above investigation, we proposed the possible catalytic mechanisms by pinpointing the active species generation (Figure 5f). The available H_2O_2 was initially catalyzed by metal ions to produce $^{\bullet}OH$, $^{\bullet}OOH$, and $^{\bullet}O_2^{-}$ [Equations (2), (6), (7) and (18)–(21), (24) and (25)], followed by releasing O_{latt} and generating O_V. Then, the O_V and subsequence $^{\bullet}OOH$ generation decomposed H_2O_2 molecules and yielded O_{ads} that could eventually convert to large numbers of oxygen bubbles being released in the solution [Equations (17), (26) and (27)] [43].

$$O_V + H_2O_2 \rightarrow H_2O + O_{ads} \tag{26}$$

$$2O_{ads} \rightarrow O_2 \tag{27}$$

Because of its intense O_2 formation, it was transferred by the photogenerated electrons (e^{-}) to produce $^{\bullet}O_2^{-}$ [Equations (9) and (10)]. Notably, the $^{\bullet}OOH$ was generated along the catalytic mechanisms, but its oxidation potential on pollutant molecules was doubtful, rather it may only act with available H_2O_2 as precursor to generate $^{\bullet}OH$, $^{\bullet}O_2^{-}$, and $^1O_2$ [Equations (7), (8) and (17)]. During the treatment, the synergistic effect of redox reactions between transformed metal ions occurred [Equations (3)–(5]) and light irradiation and/or photogenerated e^{-} also support the metal ion coexistence, which later maintained active catalytic reaction to further ROS generation [Equations (1) and (12)]. Finally, the $^{\bullet}OH$ and $^{\bullet}O_2^{-}$ can oxidize the pollutant molecules into intermediates and mineralization products [Equation (28)].

$$^{\bullet}OH/^{\bullet}O_2^{-} + \text{pollutants} \rightarrow \text{intermediates} + CO_2 + H_2O \tag{28}$$

3.4. Reusability

To examine the $Cu_{0.5}Mn_{0.5}Fe_2O_4$ reusability and stability, we conducted a four-cycle experiment using OTC as a starting substrate. Results showed that the system can maintain its high OTC degradation efficiency (>98%) through all four cycles while the TOC removal efficiency was 48% at the first cycle and continued to decrease to 23% at the last cycle (Figure 6a). This signified that $Cu_{0.5}Mn_{0.5}Fe_2O_4$ nanoparticle photocatalytic activity and magnetization were still intact after several uses. To take a full advantage of the material magnetism, in a separate tank after the oxidation process, a magnetic catalyst collection system could be designed using a magnetic field applied underneath or adjacent to the tank wall.

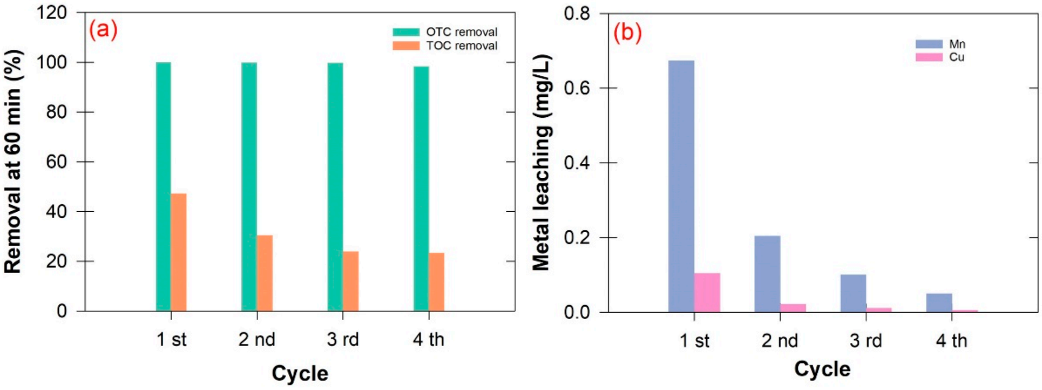

Figure 6. (**a**) OTC and TOC removal efficiency cycling test using the $Cu_{0.5}Mn_{0.5}Fe_2O_4/H_2O_2$/light system, (**b**) metal leaching concentration. (Conditions for each cycle: $[OTC]_0$ = 0.1 mM, $[H_2O_2]$ = 97.89 mM, catalyst loading = 0.5 g/L).

After each cycle, we monitored the Mn and Cu residuals and found that both metal concentrations were high in the first cycle, which was expected for the first-use catalyst, and continued to decrease in the following cycles (Figure 6b). This coincided with the higher TOC removal efficiencies in the first two cycles. We believed that metal speciation in the solution promoted the radical formations from homogeneous Fenton reaction. However, the TOC removal efficiencies for the last two cycles remained unchanged, implying the catalyst high stability, which was able to maintain its catalytic ability by the surface metal ions.

3.5. Effect of Real Wastewater

Because the metal leaching concentration from the previous recycling experiments were slightly higher than the USEPA National Secondary Drinking Water Regulations (NSDWRs), we reduced the catalyst mass to 0.2 g/L, which is less than typically reported in other references (e.g., TiO_2, ZnO; >0.5 g/L) [44]. An advantage of using less catalyst is that it would allow deeper light penetration, reduce H_2O_2 demand, and reduce possible secondary contamination. Five different water matrices spiked with OTC were used as received, and the same experimental procedure and collecting protocol were followed (Table S2). Results showed that, at this reduced catalyst dosage, almost 100% of OTC concentrations were removed within 60 min regardless of the wastewater types (Figure 7a). The TOC removal at 60 min in each wastewater revealed that TOC can only be removed by 22% to 38% while, in the control, TOC can be removed up to 52% (Figure 7a). This indicated that the wastewater had no impact on OTC degradation as it did on the TOC. The TOC removal inhibition was possibly from the presence of turbidity in the wastewater. However, changes in turbidity were obvious after treatment, supporting our treatment system as a strong oxidation technology that is also capable of decomposing natural organic matter.

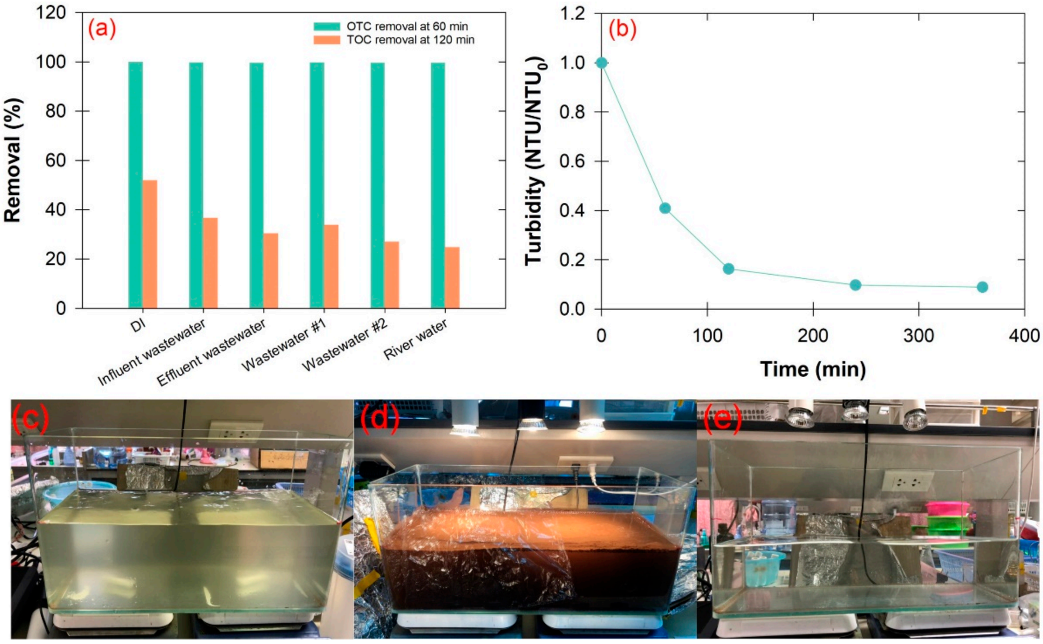

Figure 7. (**a**) Effect of real water matrices on OTC and TOC removal efficiency using the $Cu_{0.5}Mn_{0.5}Fe_2O_4$/H_2O_2/light system (Conditions: $[OTC]_0$ = 0.1 mM, catalyst loading = 0.2 g/L, $[H_2O_2]$ = 49.20 mM). (**b**) temporal changes in turbidity of real domestic wastewater using the $Cu_{0.5}Mn_{0.5}Fe_2O_4$/H_2O_2/light system, photo images of (**c**) before, (**d**) during, and (**e**) after the treatment (Conditions: catalyst loading = 0.2 g/L, $[H_2O_2]$ = 49.20 mM).

3.6. Pilot-Scale Experiment and Toxicological Evaluation

To move the technology toward commercial use, we scaled up the experimental unit by 100-fold (10 L). Pilot-scale tests were run with actual wastewater, less catalyst (minimized the catalyst loading amount by 60%) and used the treated water for further ecotoxicity testing. Results showed that turbidity was dramatically decreased within the first 2 h (85% removal) and the turbidity plateau had reached 1 nephelometric turbidity unit (NTU), which was much lower than the drinking water standard (~5 NTU) (Figure 7b). As organic matter partially corresponds to the turbidity, with this strong oxidizing process, the turbidity and dissolved organic material can then be easily removed (Figure 7c–e). We also believe that metal ion speciation in the solution and on the nanoparticle surfaces were responsible for this decrease as they existed as metal constituent ion sources (Figure 5f). These ion-exchange ions can significantly increase not only $^{\bullet}OH$ radicals but also promote the coalescence phenomenon [45]. In addition, the iron hydroxide that may be present following our photo-Fenton catalytic process can also act as a coagulant [46]. Lastly, the external magnetic force for catalyst removal may consequently facilitate the agglomeration process between the catalyst itself and other colloidal particles, thus decreasing the turbidity. While the pre-treatment is usually responsible for excess colloids and turbidity, we provided proof that using $Cu_{0.5}Mn_{0.5}Fe_2O_4$ nanoparticles would also be beneficial for removing organic pollutants as well as the available turbidity.

Because only a minimal amount of treated water is usually mixed with a large amount of receiving water, we assessed the toxicological effects on the submerged macrophytes (*Hydrilla verticillata*) and the changes in the zooplankton community. The *Hydrilla verticillata* leaves were more sensitive to treated water than the stem in all conditions while the control of healthy *Hydrilla verticillata* revealed its intact leaves (Figure 8a). After 5 d of exposure, microscopic observation revealed thin cuticles on the epidermis layer, which likely resulted from the first contact with active radicals (Figure 8b). Change in the leaf surface morphology, loss of chlorophyll pigments, and increase in the air pocket in the epidermal cells, are even more obvious at higher treated water composition, signaling the plant stress from the residual H_2O_2 and possibly from some of the reactive oxygen species (ROS) [47]. Notably in 5% treated water, after only 10 d of exposure, we observed leaf regeneration along the entire stem length, and all old leaves were detached and substituted with the new ones. This can be explained by the fact that the available ROS and H_2O_2 can only harm the plants in the beginning phase, supporting our catalytic system as an environmentally friendly treatment technology.

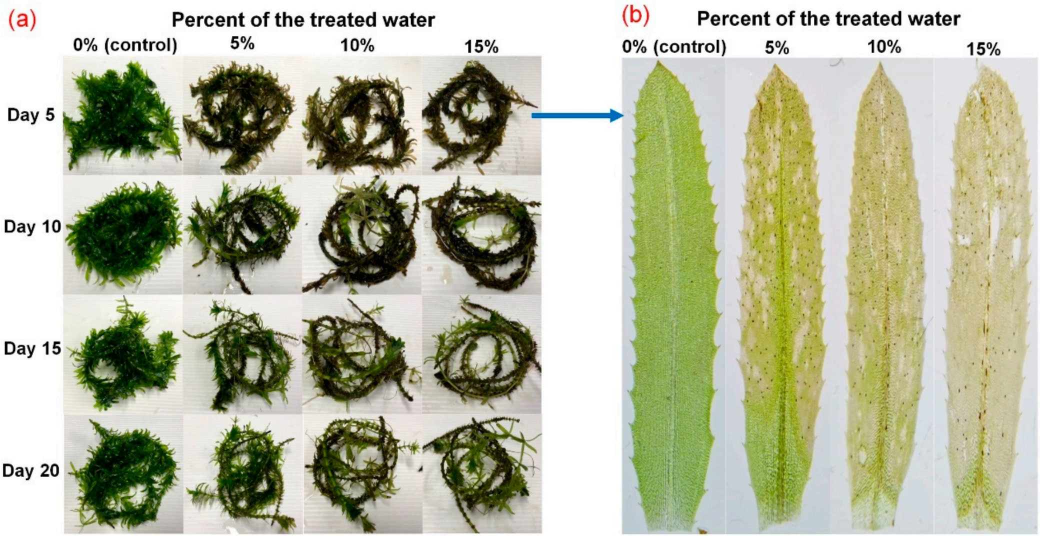

Figure 8. (**a**,**b**) Images of *Hydrilla verticillata* changes after exposure to different percentages of the treated water (0–15%).

Because zooplanktons are representative bio-indicators for the aquatic ecosystem and can be used to evaluate the water pollution levels, we further investigated changes in the zooplankton community and acclimatized them as a starting substrate. From the natural habitat from the wastewater (Wastewater Collection Station #3), the control (i.e., no treated water) existed four genera, three genera, and one genus from three phyla (i.e., Arthropoda, Rotifera, and Protozoa) (Figure 9a). Among these, Arthropoda was the dominant phylum, and the *Cyclopoid copepod* (99 Ind/L) was numerically dominant among the other zooplankton in the control experiment (Figure 9b). After exposure to 5% treated water, the Arthropoda total amount decreased by 41% and continued to decrease at higher mixed ratios (10%, 15%). Moreover, *Daphnia* and *Moina* were the sensitive genera as they drastically decreased from the community, corresponding to the previous report that the H_2O_2 concentration at >0.04 g/L can cause tissue damage to *Daphnia* and *Moina* with acute exposure [48]. Conversely, Rotifera was the dominant phylum after exposure, constituting 73% of the zooplankton abundance, which also accounted for a dramatic increase in rotifers (12 Ind/L; 0% vs. 399 Ind/L; 5%) (Figure 9a,b). *Brachionus* and *Anuraeiopsis* were the two genera with the highest tolerance to the foreign chemicals which can be explained from their persistent behavior in drastic environmental conditions as compared to other general genera in the Arthropoda phylum such as *Moina*, and *Copepod* [49,50]. As Rotifera are known to exist in the Limnosaprobity quadrant, a slight increase in dissolved oxygen from the available H_2O_2 can support the growing phase of these local rotifers. In addition, the residual H_2O_2 may be beneficial to these rotifers as it may be capable of decomposing available organic matter that was suitable for the rotifer uptake, yet not sufficient to harm rotifers. This also coincided with the sudden decrease of *Brachionus* and *Anuraeiopsis* genera as well as the smaller number of zooplankton and their number of genera at higher exposure to treated water (>5%) (Figure 9a–c).

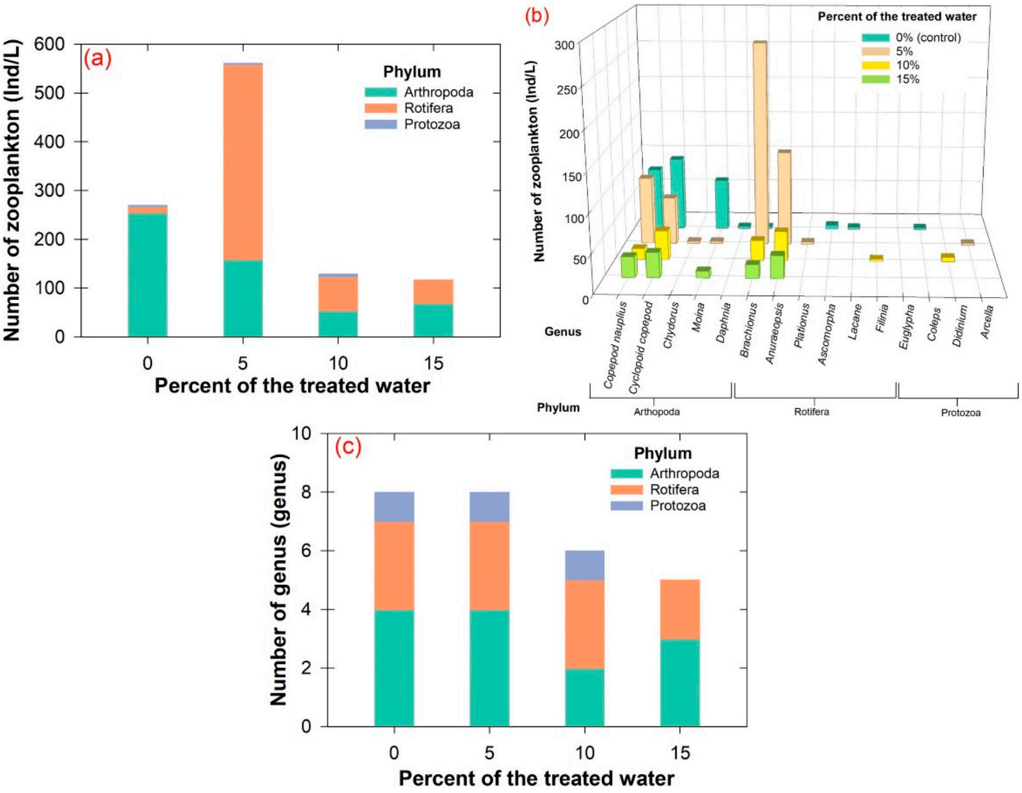

Figure 9. (**a**) Changes in number of zooplankton categorized by phylum, (**b**) categorized by genus, and (**c**) changes in number of genera after exposure to different percentages of the treated water (0–15%).

Overall results showed that although our photocatalytic system was able to remove organic residuals, the treated water still retains some oxidative species that can have a slight impact on small organisms in aquatic ecosystems. However, this unstable H_2O_2 may not be too problematic to the environment as long as treated water is retained in the maturation tank to ensure the H_2O_2 dissipation under sunlight. Most importantly, in the real-world application, the treated water composition in the natural water body may be much less than 5% as demonstrated in the toxicological assessment in this study.

4. Conclusions

In summary, magnetic recoverable $Cu_{0.5}Mn_{0.5}Fe_2O_4$ nanoparticles were successfully synthesized by coprecipitation followed by melamine-assisted calcination methods. Melamine addition during the calcination process served as a coordinating agent that reduced α-Fe_2O_3 impurity and promoted the spinel ferrite structures. Cu-substitution in the $MnFe_2O_4$ structure effectively reduced agglomeration, thus providing a higher active surface area and also promoting photo-Fenton catalytic activities through surface Cu ions and the synergistic effect between Mn-Cu-Fe valences. By using $Cu_{0.5}Mn_{0.5}Fe_2O_4$, several organic pollutant concentrations decreased by 87.6% to 100% while TOC content decreased by 28.2% to 67.9% within 120 min. Quenching experiments revealed that $^{\bullet}OH$ and $^{\bullet}O_2^{-}$ were predominant reactive species and the photogenerated e^{-} also promoted the active radical formations. XPS analysis of fresh and used $Cu_{0.5}Mn_{0.5}Fe_2O_4$ nanoparticles confirmed the metal ion transformation roles in the radical formation mechanism. $Cu_{0.5}Mn_{0.5}Fe_2O_4$ nanoparticles showed excellent photo-Fenton catalytic ability in different water samples and high stability after use for many cycles. Our developed system can decompose not only soluble pollutants but also effectively remove colloids in water. Treated water at different composition ratios (5–15%) had a significant impact on the *Hydrilla verticillata* leaves at the beginning phase and leaf regeneration was observed after 10 d of exposure. The number of surviving zooplankton significantly reduced when exposed to 10% and 15% of the treated water, but rotifer numbers increased when exposed to 5% of the treated water. Overall results reveal that the $Cu_{0.5}Mn_{0.5}Fe_2O_4/H_2O_2$/light system is an efficient and environmentally friendly system for degrading a variety of organic contaminants.

Supplementary Materials: The following supporting information can be downloaded at: https://www.mdpi.com/article/10.3390/w14223717/s1, Section S1: Chemicals; Section S2: Chemical analyses; Section S3: Material characterization; Section S4: Role of melamine addition; Table S1: HPLC conditions for quantifying the concentrations of antibiotics, herbicides, and parabens; Table S2: Physical and chemical characteristics of the water samples; Figure S1: (a) scanning electron microscopy (SEM)image, X-ray mapping of (b) C, (c) O, (d) Mn, (e) Fe, (f) Cu, and (g) spectrum of $Cu_{0.5}Mn_{0.5}Fe_2O_4$ nanoparticles; Figure S2: The $Cu_{0.5}Mn_{0.5}Fe_2O_4$ nanoparticle (a) FTIR, (b) XPS survey, (c) C 1s XPS spectra; Figure S3: (a) UV-Vis diffuse reflectance spectra (DRS), (b) $(\alpha h\nu)^2$ vs. photon energy ($h\nu$) curves of the $Cu_{0.5}Mn_{0.5}Fe_2O_4$ nanoparticles; Figure S4: Photo-Fenton catalytic degradation of MB with different composition ratios (Conditions: $[H_2O_2]$ = 97.89 mM, catalyst loading = 0.5 g/L, $[MB]_0$ = 80 mg/L); Figure S5: (a) Adsorption of various organic pollutants by $Cu_{0.5}Mn_{0.5}Fe_2O_4$ nanoparticles (Conditions: catalyst dose = 4 g/L, $[pollutant]_0$ = 0.1 mM or $[HA]_0$ = 100 mM) and (b) pH_{pzc} analysis of $Cu_{0.5}Mn_{0.5}Fe_2O_4$ nanoparticles. References [51–58] are cited in the Supplementary Materials.

Author Contributions: Conceptualization, C.S. and C.C.; data curation, A.A.; formal analysis, A.A.; funding acquisition, C.C.; investigation, A.A.; methodology, A.A. and M.N.; project administration, C.C.; resources, C.S.; supervision, C.C.; validation, A.A. and C.C.; visualization, A.A.; writing—original draft, A.A., C.S. and C.C.; writing—review & editing, C.S., S.I., T.S., N.S., T.K., S.C. and C.C. All authors have read and agreed to the published version of the manuscript.

Funding: This research was funded by the National Research Council of Thailand (NRCT) through the Royal Golden Jubilee PhD Program (Grant No: NRCT5-RGJ63002-044).

Institutional Review Board Statement: This study followed the animal research ethical approval obtained from Kasetsart University (ID# ACKU64-VTN-016).

Informed Consent Statement: Not applicable.

Data Availability Statement: The authors confirm that the data supporting the findings of this study are available within the article.

Acknowledgments: Appreciation is expressed to Apichon Watcharenwong from the School of Environmental Engineering, Institute of Engineering, Suranaree University of Technology, Thailand, for technical assistance. We graciously thank the Department of Environmental Technology and Management, Faculty of Environment, and the Faculty of Veterinary Technology, Kasetsart University, Bangkok, Thailand, for providing facility support.

Conflicts of Interest: The authors declare no conflict of interest.

References

1. Kumar, S.M. Degradation and mineralization, of organic contaminants by Fenton and photo-Fenton processes: Review of mechanisms and effects of organic and inorganic additives. *Res. J. Chem. Environ.* **2011**, *15*, 96–112.
2. Yang, Y.; Ok, Y.S.; Kim, K.-H.; Kwon, E.E.; Tsang, Y.F. Occurrences and removal of pharmaceuticals and personal care products (PPCPs) in drinking water and water/sewage treatment plants: A review. *Sci. Total Environ.* **2017**, *596–597*, 303–320. [CrossRef] [PubMed]
3. Rezaei Kalantary, R.; Barzegar, G.; Jorfi, S. Monitoring of pesticides in surface water, pesticides removal efficiency in drinking water treatment plant and potential health risk to consumers using Monte Carlo simulation in Behbahan City, Iran. *Chemosphere* **2022**, *286*, 131667. [CrossRef] [PubMed]
4. Zhou, X.; Kong, L.; Jing, Z.; Wang, S.; Lai, Y.; Xie, M.; Ma, L.; Feng, Z.; Zhan, J. Facile synthesis of superparamagnetic β-CD-$MnFe_2O_4$ as a peroxymonosulfate activator for efficient removal of 2,4- dichlorophenol: Structure, performance, and mechanism. *J. Hazard. Mater.* **2020**, *394*, 122528. [CrossRef]
5. Wang, X.; Wang, A.; Ma, J. Visible-light-driven photocatalytic removal of antibiotics by newly designed C_3N_4@$MnFe_2O_4$-graphene nanocomposites. *J. Hazard. Mater.* **2017**, *336*, 81–92. [CrossRef]

6. Lai, C.; Huang, F.; Zeng, G.; Huang, D.; Qin, L.; Cheng, M.; Zhang, C.; Li, B.; Yi, H.; Liu, S. Fabrication of novel magnetic $MnFe_2O_4$/bio-char composite and heterogeneous photo-Fenton degradation of tetracycline in near neutral pH. *Chemosphere* **2019**, *224*, 910–921. [CrossRef]
7. Peng, W.; Zhang, K.; Zong, F.; Chen, C.; Fang, Z. Enhancement of H_2O_2 decomposition by the synergistic effect on CuO-$MnFe_2O_4$ nanoparticles for sulfamethoxazole degradation over a wide pH range. *J. Dispers. Sci. Technol.* **2020**, *41*, 2211–2222. [CrossRef]
8. Wang, F.-X.; Wang, C.-C.; Du, X.; Li, Y.; Wang, F.; Wang, P. Efficient removal of emerging organic contaminants via photo-Fenton process over micron-sized Fe-MOF sheet. *Chem. Eng. J.* **2022**, *429*, 132495. [CrossRef]
9. Chen, X.; Zhang, M.; Qin, H.; Zhou, J.; Shen, Q.; Wang, K.; Chen, W.; Liu, M.; Li, N. Synergy effect between adsorption and heterogeneous photo-Fenton-like catalysis on $LaFeO_3$/lignin-biochar composites for high efficiency degradation of ofloxacin under visible light. *Sep. Purif. Technol.* **2022**, *280*, 119751. [CrossRef]
10. Li, X.; Zhang, X.; Wang, S.; Yu, P.; Xu, Y.; Sun, Y. Highly enhanced heterogeneous photo-Fenton process for tetracycline degradation by Fe/SCN Fenton-like catalyst. *J. Environ. Manag.* **2022**, *312*, 114856. [CrossRef]
11. Wang, Z.; Ma, H.; Zhang, C.; Feng, J.; Pu, S.; Ren, Y.; Wang, Y. Enhanced catalytic ozonation treatment of dibutyl phthalate enabled by porous magnetic Ag-doped ferrospinel $MnFe_2O_4$ materials: Performance and mechanism. *Chem. Eng. J.* **2018**, *354*, 42–52. [CrossRef]
12. Wang, Z.; Lai, C.; Qin, L.; Fu, Y.; He, J.; Huang, D.; Li, B.; Zhang, M.; Liu, S.; Li, L.; et al. ZIF-8-modified $MnFe_2O_4$ with high crystallinity and superior photo-Fenton catalytic activity by Zn-O-Fe structure for TC degradation. *Chem. Eng. J.* **2020**, *392*, 124851. [CrossRef]
13. Angkaew, A.; Chokejaroenrat, C.; Sakulthaew, C.; Mao, J.; Watcharatharapong, T.; Watcharenwong, A.; Imman, S.; Suriyachai, N.; Kreetachat, T. Two facile synthesis routes for magnetic recoverable $MnFe_2O_4$/g-C_3N_4 nanocomposites to enhance visible light photo-Fenton activity for methylene blue degradation. *J. Environ. Chem. Eng.* **2021**, *9*, 105621. [CrossRef]
14. Huang, G.-X.; Wang, C.-Y.; Yang, C.-W.; Guo, P.-C.; Yu, H.-Q. Degradation of Bisphenol A by Peroxymonosulfate Catalytically Activated with $Mn_{1.8}Fe_{1.2}O_4$ Nanospheres: Synergism between Mn and Fe. *Environ. Sci. Technol.* **2017**, *51*, 12611–12618. [CrossRef]
15. Yang, L.; Zhang, Y.; Liu, X.; Jiang, X.; Zhang, Z.; Zhang, T.; Zhang, L. The investigation of synergistic and competitive interaction between dye Congo red and methyl blue on magnetic $MnFe_2O_4$. *Chem. Eng. J.* **2014**, *246*, 88–96. [CrossRef]
16. Velinov, N.; Petrova, T.; Tsoncheva, T.; Genova, I.; Koleva, K.; Kovacheva, D.; Mitov, I. Auto-combustion synthesis, Mössbauer study and catalytic properties of copper-manganese ferrites. *Hyperfine Interact.* **2016**, *237*, 1–11. [CrossRef]
17. Zhan, Y.; Meng, Y.; Li, W.; Chen, Z.; Yan, N.; Li, Y.; Teng, M. Magnetic recoverable $MnFe_2O_4$/cellulose nanocrystal composites as an efficient catalyst for decomposition of methylene blue. *Ind. Crops Prod.* **2018**, *122*, 422–429. [CrossRef]
18. Zhao, W.; Wei, Z.; Zhang, X.; Ding, M.; Huang, S.; Yang, S. Magnetic recyclable $MnFe_2O_4$/CeO_2/SnS_2 ternary nano-photocatalyst for photo-Fenton degradation. *Appl. Catal. A Gen.* **2020**, *593*, 117443. [CrossRef]
19. Rana, M.U.; Misbah-ul-Islam; Abbas, T. Magnetic interactions in Cu-substituted manganese ferrites. *Solid State Commun.* **2003**, *126*, 129–133. [CrossRef]
20. Wu, K.; Wang, M.; Li, A.; Zhao, Z.; Liu, T.; Hao, X.; Yang, S.; Jin, P. The enhanced As(III) removal by Fe-Mn-Cu ternary oxide via synergistic oxidation: Performances and mechanisms. *Chem. Eng. J.* **2021**, *406*, 126739. [CrossRef]
21. Sun, Y.; Zhou, J.; Liu, D.; Li, X.; Liang, H. Enhanced catalytic performance of Cu-doped $MnFe_2O_4$ magnetic ferrites: Tetracycline hydrochloride attacked by superoxide radicals efficiently in a strong alkaline environment. *Chemosphere* **2022**, *297*, 134154. [CrossRef]
22. Meena, S.; Renuka, L.; Anantharaju, K.S.; Vidya, Y.S.; Nagaswarupa, H.P.; Prashantha, S.C.; Nagabhushana, H. Optical, Electrochemical and Photocatalytic Properties of Sunlight Driven Cu Doped Manganese Ferrite Synthesized by Solution Combustion Synthesis. *Mater. Today Proc.* **2017**, *4*, 11773–11781. [CrossRef]
23. Faria, P.C.C.; Órfão, J.J.M.; Pereira, M.F.R. Adsorption of anionic and cationic dyes on activated carbons with different surface chemistries. *Water Res.* **2004**, *38*, 2043–2052. [CrossRef] [PubMed]
24. Tadic, M.; Panjan, M.; Damnjanovic, V.; Milosevic, I. Magnetic properties of hematite (α-Fe_2O_3) nanoparticles prepared by hydrothermal synthesis method. *Appl. Surf. Sci.* **2014**, *320*, 183–187. [CrossRef]
25. Yang, J.; Zhang, Y.; Zeng, D.; Zhang, B.; Hassan, M.; Li, P.; Qi, C.; He, Y. Enhanced catalytic activation of photo-Fenton process by $Cu_{0.5}Mn_{0.5}Fe_2O_4$ for effective removal of organic contaminants. *Chemosphere* **2020**, *247*, 125780. [CrossRef]
26. Cai, C.; Zhang, Z.; Liu, J.; Shan, N.; Zhang, H.; Dionysiou, D.D. Visible light-assisted heterogeneous Fenton with $ZnFe_2O_4$ for the degradation of Orange II in water. *Appl. Catal. B Environ.* **2016**, *182*, 456–468. [CrossRef]
27. Chen, Y.; Zeng, Z.; Li, Y.; Liu, Y.; Chen, Y.; Wu, Y.; Zhang, J.; Li, H.; Xu, R.; Wang, S.; et al. Glucose enhanced the oxidation performance of iron-manganese binary oxides: Structure and mechanism of removing tetracycline. *J. Colloid Interface Sci.* **2020**, *573*, 287–298. [CrossRef]
28. Cheng, D.; Yan, C.; Liu, Y.; Zhou, Y.; Lu, D.; Tang, X.; Cai, G.; Li, D.; Zhao, Z.; Wang, X. Loading $CuFe_2O_4$ onto ceramic fabric for photocatalytic degradation of methylene blue under visible light irradiation. *Ceram. Int.* **2022**, *48*, 1256–1263. [CrossRef]
29. Utset, B.; Garcia, J.; Casado, J.; Domènech, X.; Peral, J. Replacement of H_2O_2 by O_2 in Fenton and photo-Fenton reactions. *Chemosphere* **2000**, *41*, 1187–1192. [CrossRef]
30. Hashemian, S.; Mirshamsi, M. Kinetic and thermodynamic of adsorption of 2-picoline by sawdust from aqueous solution. *J. Ind. Eng. Chem.* **2012**, *18*, 2010–2015. [CrossRef]

31. Punamiya, P.; Sarkar, D.; Rakshit, S.; Datta, R. Effectiveness of Aluminum-based Drinking Water Treatment Residuals as a Novel Sorbent to Remove Tetracyclines from Aqueous Medium. *J. Environ. Qual.* **2013**, *42*, 1449–1459. [CrossRef] [PubMed]
32. Wang, M.; Chen, K.; Liu, J.; He, Q.; Li, G.; Li, F. Efficiently Enhancing Electrocatalytic Activity of α-MnO_2 Nanorods/N-Doped Ketjenblack Carbon for Oxygen Reduction Reaction and Oxygen Evolution Reaction Using Facile Regulated Hydrothermal Treatment. *Catalysts* **2018**, *8*, 138. [CrossRef]
33. Zhou, Y.; Xiao, B.; Liu, S.-Q.; Meng, Z.; Chen, Z.-G.; Zou, C.-Y.; Liu, C.-B.; Chen, F.; Zhou, X. Photo-Fenton degradation of ammonia via a manganese–iron double-active component catalyst of graphene–manganese ferrite under visible light. *Chem. Eng. J.* **2016**, *283*, 266–275. [CrossRef]
34. Oberländer, J.; Kirchner, P.; Boyen, H.-G.; Schöning, M.J. Detection of hydrogen peroxide vapor by use of manganese(IV) oxide as catalyst for calorimetric gas sensors. *Phys. Status Solidi A* **2014**, *211*, 1372–1376. [CrossRef]
35. Lv, H.; Zhao, H.; Cao, T.; Qian, L.; Wang, Y.; Zhao, G. Efficient degradation of high concentration azo-dye wastewater by heterogeneous Fenton process with iron-based metal-organic framework. *J. Mol. Catal. A Chem.* **2015**, *400*, 81–89. [CrossRef]
36. Dai, C.; Tian, X.; Nie, Y.; Lin, H.-M.; Yang, C.; Han, B.; Wang, Y. Surface Facet of $CuFeO_2$ Nanocatalyst: A Key Parameter for H_2O_2 Activation in Fenton-Like Reaction and Organic Pollutant Degradation. *Environ. Sci. Technol.* **2018**, *52*, 6518–6525. [CrossRef] [PubMed]
37. Xiunan, C.; Ling, T.; Meifei, C.; Yijun, L.; Wei, W.; Junhao, L.; Yanjuan, Z.; Gan, T.; Huayu, H.; Zuqiang, H. Construction of a C-decorated and Cu-doped (Fe,Cu)S/$CuFe_2O_4$ solid solution for photo-Fenton degradation of hydrophobic organic contaminant: Enhanced electron transfer and adsorption capacity. *Chemosphere* **2022**, *296*, 134005. [CrossRef]
38. Zhong, Y.; Liang, X.; Zhong, Y.; Zhu, J.; Zhu, S.; Yuan, P.; He, H.; Zhang, J. Heterogeneous UV/Fenton degradation of TBBPA catalyzed by titanomagnetite: Catalyst characterization, performance and degradation products. *Water Res.* **2012**, *46*, 4633–4644. [CrossRef]
39. Chen, Z.; Bi, S.; Zhao, G.; Chen, Y.; Hu, Y. Enhanced degradation of triclosan by cobalt manganese spinel-type oxide activated peroxymonosulfate oxidation process via sulfate radicals and singlet oxygen: Mechanisms and intermediates identification. *Sci. Total Environ.* **2020**, *711*, 134715. [CrossRef]
40. Wang, R.; An, H.; Zhang, H.; Zhang, X.; Feng, J.; Wei, T.; Ren, Y. High active radicals induced from peroxymonosulfate by mixed crystal types of $CuFeO_2$ as catalysts in the water. *Appl. Surf. Sci.* **2019**, *484*, 1118–1127. [CrossRef]
41. Hao, Y.-J.; Liu, B.; Tian, L.-G.; Li, F.-T.; Ren, J.; Liu, S.-J.; Liu, Y.; Zhao, J.; Wang, X.-J. Synthesis of {111} Facet-Exposed MgO with Surface Oxygen Vacancies for Reactive Oxygen Species Generation in the Dark. *ACS Appl. Mater. Interfaces* **2017**, *9*, 12687–12693. [CrossRef] [PubMed]
42. Gao, P.; Chen, X.; Hao, M.; Xiao, F.; Yang, S. Oxygen vacancy enhancing the Fe_2O_3-CeO_2 catalysts in Fenton-like reaction for the sulfamerazine degradation under O_2 atmosphere. *Chemosphere* **2019**, *228*, 521–527. [CrossRef] [PubMed]
43. Lee, Y.N.; Lago, R.M.; Fierro, J.L.G.; González, J. Hydrogen peroxide decomposition over $Ln_{1-x}A_xMnO_3$ (Ln = La or Nd and A = K or Sr) perovskites. *Appl. Catal. A Gen.* **2001**, *215*, 245–256. [CrossRef]
44. Rueda-Marquez, J.J.; Levchuk, I.; Fernández Ibañez, P.; Sillanpää, M. A critical review on application of photocatalysis for toxicity reduction of real wastewaters. *J. Clean. Prod.* **2020**, *258*, 120694. [CrossRef]
45. Mahdad, F.; Younesi, H.; Bahramifar, N.; Hadavifar, M. Optimization of Fenton and photo-Fenton-based advanced oxidation processes for post-treatment of composting leachate of municipal solid waste by an activated sludge process. *KSCE J. Civ. Eng.* **2016**, *20*, 2177–2188. [CrossRef]
46. de Moura Gomes, L.; da Silva Duarte, J.L.; Pereira, N.M.; Martínez-Huitle, C.A.; Tonholo, J.; de Paiva e Silva Zanta, C.L. Development of a system for treatment of coconut industry wastewater using electrochemical processes followed by Fenton reaction. *Water Sci. Technol.* **2014**, *69*, 2258–2264. [CrossRef] [PubMed]
47. Al-Zurfi, S.K.L.; Alisaw, A.Y.; Al-Shafai, G.A.A. Anatomical and physiological effects of cadmium in aquatic plant *Hydrilla Verticillata*. *Plant Arch.* **2018**, *18*, 839–846.
48. Reichwaldt, E.S.; Zheng, L.; Barrington, D.J.; Ghadouani, A. Acute toxicological response of Daphnia and Moina to hydrogen peroxide. *J. Environ. Eng.* **2012**, *138*, 607. [CrossRef]
49. Jepsen, P.M.; Andersen, C.V.B.; Schjelde, J.; Hansen, B.W. Tolerance of un-ionized ammonia in live feed cultures of the calanoid copepod *Acartia tonsa* Dana. *Aquac. Res.* **2015**, *46*, 420–431. [CrossRef]
50. Arauzo, M.; Valladolid, M. Short-term harmful effects of unionised ammonia on natural populations of *Moina micrura* and *Brachionus rubens* in a deep waste treatment pond. *Water Res.* **2003**, *37*, 2547–2554. [CrossRef]
51. Huang, L.; Xu, H.; Li, Y.; Li, H.; Cheng, X.; Xia, J.; Xu, Y.; Cai, G. Visible-light-induced WO_3/g-C_3N_4 composites with enhanced photocatalytic activity. *Dalton Trans.* **2013**, *42*, 8606–8616. [CrossRef] [PubMed]
52. Huang, S.; Xu, Y.; Xie, M.; Xu, H.; He, M.; Xia, J.; Huang, L.; Li, H. Synthesis of magnetic $CoFe_2O_4$/g-C_3N_4 composite and its enhancement of photocatalytic ability under visible-light. *Colloids Surf. A Physicochem. Eng. Asp.* **2015**, *478*, 71–80. [CrossRef]
53. Ghassemi, N.; Davarani, S.S.H.; Moazami, H.R. Cathodic electrosynthesis of $CuFe_2O_4$/CuO composite nanostructures for high performance supercapacitor applications. *J. Mater. Sci. Mater. Electron.* **2018**, *29*, 12573–12583. [CrossRef]
54. Ghobadi, M.; Gharabaghi, M.; Abdollahi, H.; Boroumand, Z.; Moradian, M. $MnFe_2O_4$-graphene oxide magnetic nanoparticles as a high-performance adsorbent for rare earth elements: Synthesis, isotherms, kinetics, thermodynamics and desorption. *J. Hazard. Mater.* **2018**, *351*, 308–316. [CrossRef] [PubMed]

55. Goodgame, D.M.; Hussain, I.; White, A.J.; Williams, D.J. Synthesis and structure of a copper (II) melamine complex, [Cu(C3H6N6)(μ-OCH3)(ONO2)(HOCH3)]2, with direct Cu–melamine coordination. *J. Chem. Soc. Dalton Trans.* **1999**, 2899–2900. [CrossRef]
56. Wiles, A.B.; Bozzuto, D.; Cahill, C.L.; Pike, R.D. Copper (I) and (II) complexes of melamine. *Polyhedron* **2006**, *25*, 776–782. [CrossRef]
57. Doddamani, J.S.; Hodlur, R.M.; Rabinal, M.K. Melamine assisted large-scale and rapid synthesis of porous copper oxide nanostructures. *Emergent Mater.* **2021**. [CrossRef]
58. Ansari, S.A.; Ansari, S.G.; Foaud, H.; Cho, M.H. Facile and sustainable synthesis of carbon-doped ZnO nanostructures towards the superior visible light photocatalytic performance. *New J. Chem.* **2017**, *41*, 9314–9320. [CrossRef]